Hyperfine and vibrational structure of weakly bound levels of the lowest 1_g state of molecular $^{87}Rb_2$

Chin-Chun Tsai
Department of Physics, National Cheng-Kung University, Tainan 70101, Taiwan

T. Bergeman
Department of Physics and Astronomy, SUNY, Stony Brook, New York 11794-3800, USA

E. Tiesinga and P. S. Julienne
Joint Quantum Institute, National Institute of Standards and Technology and the University of Maryland, 100 Bureau Drive, Stop 8423, Gaithersburg, Maryland 20899-8423, USA

D. J. Heinzen
Department of Physics, University of Texas, Austin, Texas 78712, USA
(Received 27 September 2013; published 13 November 2013)

Photoassociation resonances in the $^{87}Rb_2$ 1_g state dissociating to $5\,^2S + 5^2P_{1/2}$ were produced by the excitation of colliding ^{87}Rb atoms in a far-off resonance trap. Levels down to 31 cm^{-1} below the dissociation limit were measured with resonance linewidths of 15 to 20 MHz, and have been located to a one-sigma combined systematic and statistical uncertainty of 50 MHz relative to the $5\,^2S + 5^2P_{1/2}$ limit. Electron and nuclear spins were fixed to a space-fixed axis by circularly polarized optical pumping, so that only states with total nuclear spin $I = 3$ were excited, thereby greatly simplifying the spectrum. The analysis of the data yielded hyperfine coupling parameters $A(v)$, vibrational $G(v)$, and rotational $B(v)$ parameters. The $G(v)$ parameters could be fit to an rms accuracy of about 0.01 cm^{-1} to a potential constructed from current C_3 and C_6 long-range dispersion parameters plus an *ab initio* potential that was adjusted in depth and with quadratic terms in the internuclear distance added to the inner wall.

DOI: 10.1103/PhysRevA.88.052509 PACS number(s): 33.15.Mt, 33.15.Pw, 33.20.Kf, 33.20.Vq

I. INTRODUCTION

In many cases, the most feasible pathway for the production of cold molecules from cold atoms is via molecular states tending to the lowest excited atomic states [1–4]. This is especially the case for alkali-metal-atom diatomics, presently still the most widely used species for the production of cold molecules. In most instances to date, the states employed for this purpose have been $\Omega = 0$ states, where Ω is the projection of spin and orbital angular momentum along the internuclear axis. Although the $\Omega = 0$ states are typically free of hyperfine structure, other possible pathways involve $|\Omega| = 1$ states which typically have complicated hyperfine structure. It is difficult to model the vibrational structure and to calculate Franck-Condon factors if the hyperfine structure is not analyzed.

The hyperfine structure in the photoassociation of alkali-metal dimer molecules has been noted and studied for many years, from earlier work on Na_2 [5], K_2 [6], Rb_2 [7,8], and Cs_2 [9]. Multiple potential curves for hyperfine components were displayed in Refs. [5,7,9], for example. Photoassociation to $|\Omega| = 1$ states near the lowest $^2S + {}^2P$ atomic asymptotes has also been observed in KRb [10] and RbCs [11] but remains to be analyzed quantitatively. For the Rb_2 $(1)^3\Sigma_g^+(5^2P_{1/2})$ state, hyperfine structure in the lowest vibrational levels has been observed and analyzed [12]. An extensive series of photoassociation resonances to levels of both the 1_g and 0_g^- components of this state were observed by Miller *et al.* [13], and five levels of the 0_g^- component were observed by Gardner *et al.* [14]. Higher levels, near the dissociation limit, of the $1_g(P_{1/2})$ state are the subject of the present work, but there are considerable gaps between the various data sets.

There are useful results from *ab initio* calculations by various theoretical groups [15,16]. Figure 1 shows potentials calculated by the authors of Ref. [16] in the Rb_2 energy region of interest in what follows. Typically, small adjustments in these *ab initio* potentials are needed to model experimental data to the limit of the experimental accuracy, and therefore there are continuing efforts to analyze data from the laboratory. New excitation and decay pathways are continually being found to be useful, in particular for Rb_2 [2,17–22].

A complication when studying hyperfine structure (hfs) in molecular excited states can occur when several rotation-hfs levels of the cold atom dimer ground state are populated, with undetermined population ratios. For example, the $^{85}Rb_2$ photoassociation observations reported in Refs. [23,24] consisted of data for the 0_u^+ and 1_g states. The former had no hfs and thus could easily be rotationally analyzed, while the latter exhibited complicated hfs from multiple ground-state levels, and this impeded rotational analysis. This difficulty was circumvented in experiments reported in the present work, performed several years ago at the University of Texas (Austin), when a completely polarized atomic sample was produced in an optical dipole trap. As described below, this circumstance severely limited the range of diatomic ground states present, and hence simplified the excitation spectrum.

After a discussion of the experimental methods (Sec. II), we present well-resolved hyperfine structure for 33 vibrational bands of the Rb_2 $1_g(P_{1/2})$ state. From such data, we produce fits to the vibrational energies $G(v)$, the hyperfine interaction

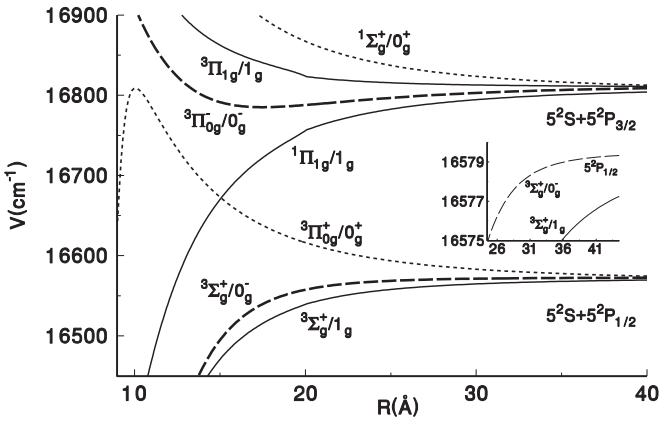

FIG. 1. Rb_2 *gerade* potentials converging to the $5\,^2S + 5\,^2P$ fine structure limits, from calculations by Aubert-Frécon [16]. The vertical scale is relative to the minimum of the $X^1\Sigma_g^+$ ground state. The data in this study are associated with the lowest potential curve shown, which has a minimum at approximately 9360 cm^{-1} on the scale of this figure. The inset shows that the splitting between the 0_g^- and 1_g states converging to the $^2P_{1/2}$ limit is calculated to be more than 1 cm^{-1} out to 45 Å.

parameters $A(v)$, and the rotational parameters $B(v)$, for each vibrational level. The hyperfine Hamiltonian and the quality of the fit to hyperfine structure are shown in Sec. III. Two approaches are used to fit potential parameters to the $G(v)$ data. As discussed in Sec. V, our first approaches, since the data are from the long range regime in the internuclear distance R, are various "near-dissociation expansion" (NDE) methods developed by the authors of Ref. [25] and refined in Ref. [26]. The NDE fit results, however, do not model the data as accurately as a fit to a numerically computed potential, our second approach. For this approach, the potential is adapted from an *ab initio* calculation [16], modified by a long-range part based on couplings between the three *gerade* states converging to $5\,^2S + 5^2P$ atoms, using accepted dispersion coefficients, and small harmonic corrections to obtain an improved fit to the present data and also to the data of the authors of Ref. [12]. Because data are very sparse for vibrational levels between $v = 16$ [12] and our own data beginning at approximately $v = 180$, there is no hope that this potential yields energy levels of spectroscopic accuracy over this intermediate region. We do obtain respectable agreement with our data near the dissociation limit, and find that the dissociation limit fitted with this model is close to the weighted average over atomic hyperfine levels.

II. EXPERIMENT

The experiment is similar to that of Ref. [14]. The data were obtained with a far-off resonance trap (FORT) employing one fixed frequency laser, plus a second laser with a 1-MHz bandwidth, to scan over the photoassociation resonances. Each cycle of photoassociation consists of trapping, loading of atoms, photoassociation, and probing the atoms remaining in the trap. To load the ^{87}Rb atoms, a magnetooptical trap (MOT) was turned on for 400 ms to grab atoms from background vapor inside an ultrahigh vacuum chamber, then the MOT and FORT laser beams were chopped at 200 kHz to further load the atoms into the FORT. The FORT laser beam was a linear polarized, Gaussian beam of about 1.5 W, focused to a waist of about 11 μm. About 10^4 atoms were loaded into the FORT. During the photoassociation period, the FORT and photoassociation laser beams were alternated at 200 kHz for 200 ms. The FORT laser was turned on for 2.5 μs in each period to keep atoms trapped. The photoassociation experiment was performed in the following 2.5 μs (FORT off) to eliminate the power broadening and frequency shifts due to the intense field of the FORT laser. During the photoassociation period, two optical pumping beams, linear polarized $5\,^2S_{1/2}(F = 1) \rightarrow 5\,^2P_{3/2}(F = 2)$ and circular polarized $\sigma^+ 5\,^2S_{1/2}(F = 2) \rightarrow 5\,^2P_{3/2}(F = 2)$ were turned on for 0.6 μs to maintain the atoms in their doubly spin-polarized ^{87}Rb $5\,^2S_{1/2}(F = 2, M_F = 2)$ sublevel, followed by a photoassociation laser beam for 1.9 μs. At the end of each 200-ms photoassociation time, a probe laser was on for 1 ms to measure the atoms remaining in the trap by laser-induced fluorescence. To obtain a spectrum as shown in Fig. 2, the cycle of loading, photoassociation, and probe are repeated for a succession of photoassociation laser frequencies (1 MHz/step). Resonances were detected by reductions in the atomic fluorescence (trap loss) when

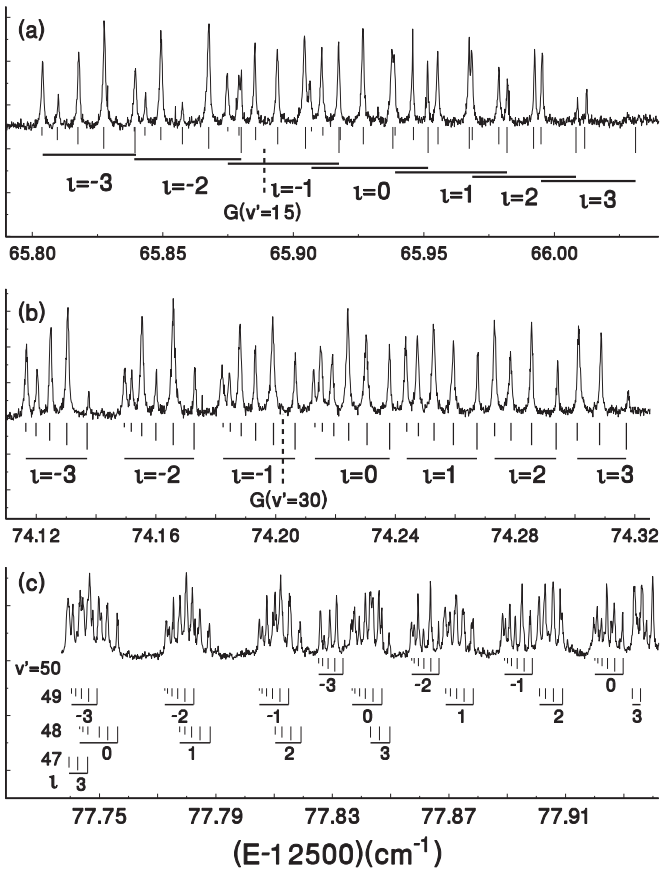

FIG. 2. Examples of photoassociation spectra, to levels of the Rb_2 1_g state below the $5\,^2S + 5\,^2P_{1/2}$ limit. Depending on the relative magnitudes of $\Delta G(v)$, $A(v)$, and $B(v)$, there can be overlap between transitions to different ι states as in (a), or to different vibrational levels, as in (c), or no overlap, as in (b). Within each ι manifold, the F values are denoted by the length of the vertical lines beneath the spectra. In (c), the numbers below the thick horizontal solid lines denote the ι values.

photoassociation occurred. A transmission signal of the photoassociation laser beam through a thermally stabilized 300 MHz free spectral range etalon was used to correct nonlinearities of the laser frequency scan. The absolute frequency of the photoassociation laser was calibrated with a scanning Michelson interferometer wavemeter with an accuracy of ±50 MHz, with the help of a frequency-stabilized HeNe laser.

A notable feature of these particular experiments was that the $5\,^2S$ ^{87}Rb atoms were doubly polarized: the electron and nuclear spins are fixed to a space-fixed axis. The binary collisions therefore produced a total nuclear spin I equal to $3/2+3/2=3$. The nuclear spin cannot change during the absorption, and hence only $I=31_g$ $^2S+^2P$ atoms are formed. The atoms have a well-defined projection of I in the space-fixed coordinate system. Nevertheless all projections ι on the body-fixed internuclear axis are observable.

III. THEORY

A. Relevant electronic structure

The structure of electronic states associated with $^2S+^2P$ alkali-metal atoms was formulated in general many years ago by Movre and Pichler (MP) [27]. In this (MP) model, there is an adiabatic recoupling of electronic degrees of freedom from a molecular coupling scheme at small internuclear separation R to an atomic one at large internuclear separation. The multichannel Hamiltonian in the MP [27] model is composed of the atomic spin-orbit Hamiltonian of the ^2P atom, which dominates at large R, and the $1/R^3$ resonant-dipole interaction, which dominates at smaller R. The resonant dipole interaction is diagonal in the molecular basis $|\Lambda,S,\Sigma\rangle_\sigma$ while the spin-orbit interaction is diagonal in the atomic basis $|(j_a,j_b)j\Omega\rangle_\sigma$. Here $\vec{L}=\vec{\ell}_a+\vec{\ell}_b$ is the total electronic angular momentum, and Λ is its projection on the internuclear axis. Similarly, $\vec{S}=\vec{s}_a+\vec{s}_b$ s the total spin angular momentum, and Σ its projection on the internuclear axis; $\vec{J}=\vec{j}_a+\vec{j}_b$ is the total electronic angular momentum and $\Omega=\Lambda+\Sigma$ its projection on the internuclear axis. $\vec{j}_\alpha=\vec{\ell}_\alpha+\vec{s}_\alpha$ is the total electronic angular momentum of one of the atoms. For a $^2P+{}^2S$ dimer, $\ell_a=1,\ell_b=0,s_a=s_b=1/2$, where the subscript $a(b)$ labels the $P(S)$ atom, respectively. Finally, the label $\sigma=g,u=$ *gerade,ungerade* describes the symmetry of the electronic wave function under inversion of the electrons through the center of charge [28], which is basically due to the degeneracy of the states $P+S$ and $S+P$ for homonuclear dimers.

For homonuclear species, there are singlet and triplet Π and Σ states of g and u parity. For excitations from the $X^1\Sigma_g^+$ ground state the most accessible states are the $A^1\Sigma_u^+$ and $B^1\Pi_u$ states, and also levels of $b^3\Pi_u$ that are intermixed with $A^1\Sigma_u^+$ levels by spin-orbit effects. For Rb_2, these states have been studied up to certain energy levels [22,29]. But possible excitations from cold atoms and from Feshbach resonance states that include components of the $a^3\Sigma_u^+$ state offer pathways to excited g states, such as those of interest in this study. From *ab initio* calculations, Fig. 1 gives a view of the g states close to the dissociation limit for which data are presented here. These potentials come primarily from electron-electron Coulomb and exchange interactions, while spin-orbit effects account for the fine-structure splitting. At large R, when spin-orbit effects become large compared to other potential terms, the Hund's case (c) notation, $\Omega_\sigma^\pm$ is more useful than the $^S\Lambda_{\Omega,\sigma}$ notation useful for smaller R. And to denote vibrational levels, the symbol v is added in this work.

For $\Omega=1_g$ symmetry which is of interest here, the adiabatic electronic eigenstates become an R-dependent linear combination of the $|\Lambda S\Sigma\rangle_g$ or alternatively $|(j_aj_b)j\Omega\rangle_g$ states. The R-dependent eigenstates are composed of three atomic basis states

$$|1_g,i;R\rangle = a_{ig}(R)|(1/2,1/2)11\rangle_g + b_{ig}(R)|(3/2,1/2)11\rangle_g + c_{ig}(R)|(3/2,1/2)21\rangle_g, \quad (1)$$

where the label $i=1$, 2, or 3 is an energy-ordered index to the adiabats and $a_{ig}^2+b_{ig}^2+c_{ig}^2=1$. Figure 1 shows the three long-range adiabatic potentials for ^{87}Rb 1_g symmetry as well as other g states dissociating to $5\,^2S+5\,^2P$ atoms. The electronic eigenfunction of the lowest adiabat of Fig. 1 reduces to $|1_g,1;R\rangle=|(1/2,1/2)11\rangle_g$ in the limit that the binding energy is small compared to the $5\,^2P$ spin-orbit splitting of 237.6 cm^{-1} [30], and at short distances turns into the $^3\Sigma_g$ adiabatic Born-Oppenheimer state.

B. Hyperfine and rotational interactions

The molecular hyperfine features of the long-range molecules are due to atomic hyperfine interactions. The hyperfine Hamiltonian is the sum of the Fermi-contact term $a_{hf,S}\vec{s}_b\cdot\vec{i}_b$ for the ^2S and the weaker dipolar hyperfine interactions included via the effective Hamiltonian $a_{hf,Pj_a}\vec{j}_a\cdot\vec{i}_a$ [31], for the ^2P atom. The ^2P atom has a different hyperfine constant for $^2P_{3/2}$ and $^2P_{1/2}$ states. For ^{87}Rb, the nuclear spin is $i_a=i_b=3/2$. The extremely weak hyperfine quadrupole interactions that are also present in a $^2P_{3/2}$ atom play no role.

The hyperfine Hamiltonian is most conveniently evaluated in the body-fixed basis $|\Omega_g,iv\rangle|(i_ai_b)I\iota\rangle$, where i is as in Eq. (1) and ι is the projection of the total nuclear spin I along the internuclear axis. The only relevant matrix elements of the hyperfine Hamiltonian in this basis are those that satisfy $\Delta I=0$ and $\Delta\iota=0$. Other matrix elements, such as those with $\Delta I=1$ are zero since only odd or even values of I mix for homonuclear dimers, or yield small corrections that mix different Hund's case (c) symmetries. For example, $\Delta\iota=1$ matrix elements mix the 1_g symmetry with the 0_u^+. With this in mind, it turns out that the hyperfine Hamiltonian is diagonal in the above basis and is given by

$$\langle\Omega_g,iv|\langle(i_ai_b)I\iota|H_{hf}|\Omega_g,iv\rangle|i_ai_b)I\iota\rangle = A(v)\Omega\iota, \quad (2)$$

where $A(v)$ is the molecular hyperfine constant which for $\Omega_\sigma=1_g$ is given by

$$\begin{aligned} A(v) &= \frac{1}{2}\langle 1_g,iv|H_{hf}|1_g,iv\rangle \\ &= \langle v|\left[\frac{1}{4}a_{i,g}^2(R)-\frac{1}{8}b_{i,g}^2(R)-\frac{\sqrt{3}}{4}b_{i,g}(R)c_{i,g}(R)\right. \\ &\quad \left.+\frac{1}{8}c_{i,g}^2(R)\right]a_{hf,S}+\frac{1}{4}a_{i,g}^2(R)a_{hf,P1/2} \end{aligned}$$

$$+\left[\frac{1}{8}b_{i,\sigma}^2(R)+\frac{\sqrt{3}}{4}b_{i,g}(R)c_{i,g}(R)+\frac{3}{8}c_{i,g}^2(R)\right]\times a_{hf,P3/2}|v\rangle. \quad (3)$$

For the vibrational levels of the 1_g adiabat near the $^2P_{1/2}+{}^2S$ asymptote this expression reduces to $(a_{hf,S}+a_{hf,P1/2})/4$ independent of v. For ^{87}Rb this constant is 0.03180 cm^{-1}.

The rotation of the atoms around their center of mass introduces the mechanical nuclear angular momentum ℓ, which points perpendicular to the internuclear axis. The vector sum of all spins, the total spin, $\vec{F}=\vec{\ell}+\vec{j}+\vec{I}$, is conserved in a space-fixed or laboratory coordinate system with what we will denote quantum numbers F and projection M. On the other hand, for the electronic and hyperfine interactions, the projections of total electronic spin Ω and the total nuclear spin ι with respect to the internuclear axis are good quantum numbers. This also implies that the projection of F on the internuclear axis $\phi=\Omega+\iota$ is conserved for the electronic and hyperfine terms of the Hamiltonian. The basis that captures both aspects uses solutions of the rigid rotor problem, i.e., the Wigner rotation matrices $D^F_{M\phi}(\alpha,\beta,\gamma)$ where F,M, and ϕ label the basis elements and α,β, and γ are the Euler angles. Wigner rotation matrices have been used to discuss atomic photoassociation and photodissociation in Refs. [32–34].

Thus the basis in which the rotation is evaluated is

$$|\Omega_g,iv I\iota FM\phi\rangle\equiv\sqrt{\frac{2F+1}{8\pi^2}}D^{F*}_{M\phi}(\alpha,\beta,\gamma)|\Omega_g,iv\rangle|(i_ai_b)I\iota\rangle. \quad (4)$$

The rotational Hamiltonian, which is given by $\hbar^2\vec{\ell}^2/2\mu R^2=\hbar^2(\vec{F}-\vec{j}-\vec{I})^2/2\mu R^2$, is not diagonal. It is given by

$$\langle\Omega_g,iv I'\iota' FM\phi'|\frac{\hbar^2\vec{\ell}^2}{2\mu R^2}|\Omega_g,iv I\iota FM\phi\rangle = \epsilon_{vg}^{j^2}+[F(F+1)+I(I+1)-\phi^2-\Omega^2-\iota^2]B_v \quad (5)$$

for the diagonal matrix elements $\iota=\iota',I=I'$, and

$$\sqrt{F(F+1)-\phi\phi'}\sqrt{I(I+1)-\iota\iota'}B_v \quad (6)$$

for the off-diagonal matrix elements $\iota'=\iota+1,\phi'=\phi+1$ or $\iota'=\iota-1,\phi'=\phi-1,I'=I$, where $B_v=\langle v|\hbar^2/2\mu R^2|v\rangle$ is the rotational constant, and

$$\epsilon_{vg}^{j^2}=\langle\Omega_g,iv|\frac{\hbar^2\vec{j}^2}{2\mu R^2}|\Omega_g,iv\rangle. \quad (7)$$

The terms in $(\vec{F}-\vec{j}-\vec{I})^2$ that lead to nonzero off-diagonal matrix elements $F_+\cdot I_-$ and $F_-\cdot I_+$ mix different ι's (or ϕ's) for a given nuclear spin I and vibrational level of a Hund's case (c) symmetry, have been neglected. The $F_\pm$ are raising and lowering operators. In evaluating Eq. (6) in a body-fixed frame, the raising and lowering operators of $\vec{F}$ have *anomalous* commutation relations [34]. In fitting the data, we include the term ϵ^{j^2} with $|\vec{j}|=2$. The rotational coupling between Hund's case (c) symmetries, that arises from cross terms like $F_+\cdot j_-$ and $j_+\cdot I_-$, has also been neglected.

IV. RESULTS

A. Hyperfine and rotational structure

Figure 2 gives examples of scans over individual or overlapping vibrational levels. Resonance positions were extracted from the data scans by fitting each resonance peak to a Gaussian function. We begin our analysis by assigning rotational and hyperfine structure transitions within a given vibrational level. These transitions are fit by optimizing values of $G(v),A(v)$, and $B(v)$. Often an additional nonlinear term, $\eta(v)(\iota+3)^2$ was included in the parameter set to minimize slight distortions in the scan. In this part of the analysis, the rms deviation of observed minus fitted line positions was 4 MHz in the best cases, and as much as 20 MHz or even 60 MHz in less favorable cases, with overlapping resonances or vibrational levels that span more than one individual laser scan.

The vertical lines below the data in Fig. 2 are at energies corresponding to the results of fitting the resonances in each band to the Hamiltonian expressions given above. Within each cluster for a given value of ι, of three to six lines, the line length is proportional to the value of the total angular momentum F. By comparison to the data, the vertical lines show the quality of the fit to the $G(v),A(v)$, and $B(v)$ parameters for each vibrational level. The middle scan in Fig. 2 shows a case in which the ι clusters are separated; in the top scan they overlap. The bottom scan shows an example in which several bands partially overlap. Beyond the level we have designated $v'=50$, the component lines are too dense to assign reliably.

Estimates of the absolute vibrational numbering, discussed below, indicate that $v'=0$ corresponds to $v=176$ to 180. The uncertainty arises from the large gap between our data and that of Ref. [12], which extends only to $v=15$. The experimental scans happened to skip over certain wavelength regions, hence the v' numbers are not continuous.

A complete tabulation of the observed and fitted lines is given in Ref. [35], and the resulting best fit $G(v'),B(v'),A(v')$, and $\eta(v')$ parameters are displayed in Table I. The error limits in parentheses are conservatively given as three standard deviations for each fitted parameter. The absolute accuracy of the $G(v)$ values is ±50 MHz, as determined by the laser frequency measurement uncertainty. while for many cases, the quoted 3σ uncertainty is only 3 MHz. A plot of the fitted hyperfine parameters $A(v)$, shown in Fig. 3, displays an evolution toward the value calculated from the atomic hyperfine parameters, as given below Eq. (3). The rotational parameters $B(v)$ are plotted in Fig. 4. Scatter in the $A(v)$ and $B(v)$ values, beyond the three σ uncertainties, reflects the effects of perturbations by states of various other symmetries, which presently are not accurately characterized in this energy region. Fragmentary observations, such as three extra lines in the data for $v'=30$ (shown in Ref. [35]), are clearly inadequate to characterize the perturbing states. These undetermined, fluctuating, perturbation effects induce us to quote 3σ uncertainties, rather than 1σ or 2σ values in Table I and Figs. 3 and 4.

B. Vibrational structure of the $1_g(^2P_{1/2})$ State

For molecular vibrational energy levels near a dissociation limit, near dissociation expansion (NDE) semiclassical

TABLE I. Results from the least-squares fits to individual bands, and results of various fits to the vibrational structure. All data are in cm^{-1}. Here $E_0 = 12\,500$ cm^{-1}, and energies are relative to the $5\,^2S, F = 2 + 5\,^2S, F = 2$ diatomic hyperfine level, as in the experiments. The $v' = 0$ in the first column corresponds approximately to $v = 176$–180, as discussed in the text. The second column gives the number of hfs peaks in the fit, and the third column gives the rms residual in MHz. Numbers in parentheses for $G(v)$, $B(v)$, and $A(v)$ give three times the standard deviation from the fitting program. The column labeled "δ_{pf}" shows deviations (calculated minus observed) from a fit to a numerically computed potential, as discussed in the text. The columns labeled δ_a and δ_b show the results of a NDE fit with C_3 only, and with C_6 also, respectively (see text). For δ_b, the residuals are calculated from deviations in the fit to $v - v_D$ and the calculated value of dE/dv. Deviations marked with an asterisk (in δ_a) were not included in the fit, but are presented to show the quality of the fit for lower-energy $G(v')$ values.

v'	np	rms	$G(v')-E_0$	δ_{pf}	$10^4 B(v')$	$10^2 A(v')$	$10^4\eta$	δ_a	δ_b
0	28	5.6	47.1804(1)	0.0001	20.11(4)	3.010(7)	0.3(1)	−2.1527*	−0.1278
1	30	6.2	48.8917(1)	0.0013	19.34(4)	2.940(7)	1.0(1)	−1.9531*	−0.0843
5	30	5.2	54.9990(1)	0.0011	16.86(4)	2.983(6)	0.2(1)	−1.2867*	0.0453
6	31	5.1	56.3530(1)	0.0004	16.30(3)	2.970(6)	0.7(1)	−1.1510*	0.0667
14	31	12.0	65.0357(2)	0.0036	12.34(8)	3.002(12)	0.2(2)	−0.4010*	0.1362
15	30	5.5	65.8848(1)	0.0054	12.09(4)	2.992(6)	1.1(1)	−0.3422*	0.1343
19	34	6.7	68.9040(1)	−0.0444	10.47(4)	3.030(7)	1.4(1)	−0.2417*	0.0315
20	30	63.5	69.5016(12)	0.0011	9.09(39)	3.135(65)	−2.8(8)	−0.1413*	0.0943
26	26	21.4	72.6530(4)	0.0063	7.40(14)	2.992(23)	0.5(3)	−0.0209	0.0364
27	34	7.5	73.0739(1)	0.0088	7.54(4)	3.014(7)	1.8(1)	−0.0032	0.0339
28	34	5.1	73.4693(1)	0.0113	7.25(3)	3.002(5)	2.1(1)	0.0052	0.0241
29	33	21.9	73.8451(1)	0.0092	6.42(13)	3.045(21)	−0.5(3)	0.0131	0.0159
30	35	3.5	74.1997(1)	0.0053	6.47(2)	2.970(3)	1.0(1)	0.0072	−0.0040
31	34	5.9	74.5302(1)	0.0037	6.21(3)	3.006(5)	0.7(1)	0.0060	−0.0172
32	35	5.0	74.8420(1)	0.0002	6.07(3)	3.090(5)	0.5(1)	−0.0033	−0.0365
33	35	4.9	75.1291(1)	0.0019	5.82(3)	3.046(4)	1.5(1)	0.0044	−0.0370
34	26	6.6	75.4008(1)	0.0004	5.62(4)	3.115(9)	0.6(1)	−0.0009	−0.0487
35	35	3.9	75.6529(1)	0.0012	5.33(2)	3.078(4)	1.1(1)	0.0026	−0.0498
36	35	6.0	75.8890(1)	0.0014	5.13(3)	3.112(5)	0.9(1)	0.0037	−0.0517
37	35	6.7	76.1099(1)	0.0012	4.92(4)	3.128(6)	1.2(1)	0.0041	−0.0527
38	33	8.4	76.3155(1)	0.0016	4.63(5)	3.065(8)	1.4(1)	0.0052	−0.0513
39	35	8.6	76.5103(1)	−0.0010	4.43(5)	3.154(8)	0.4(1)	−0.0083	−0.0628
40	33	18.1	76.6882(1)	0.0002	4.18(4)	3.039(6)	2.6(1)	0.0075	−0.0436
41	31	17.8	76.8561(3)	−0.0009	4.28(11)	3.159(18)	0.2(3)	−0.0112	−0.0570
42	35	8.3	77.0091(1)	0.0013	3.79(4)	3.022(7)	2.8(1)	0.0099	−0.0292
43	35	13.8	77.1564(2)	−0.0017	3.64(8)	3.095(13)	1.2(2)	−0.0090	−0.0394
44	27	17.7	77.2901(3)	−0.0014	3.35(11)	3.050(19)	0.9(2)	−0.0037	−0.0238
45	29	20.0	77.4185(4)	−0.0053	3.12(12)	3.207(19)	−1.1(2)	−0.0321	−0.0397
46	31	4.1	77.5296(1)	−0.0011	3.09(2)	3.017(4)	2.6(1)	0.0079	0.0139
47	35	20.6	77.6393(3)	−0.0039	2.73(12)	3.186(19)	−0.1(2)	−0.0127	0.0098
48	35	17.4	77.7350(3)	−0.0007	3.04(9)	3.096(14)	1.1(2)	0.0269	0.0670
49	35	17.5	77.8296(3)	−0.0038	2.57(8)	3.077(14)	2.0(2)	−0.0117	0.0498
50	35	15.5	77.9131(3)	−0.0029	2.47(9)	3.060(14)	0.6(2)	0.0133	0.0974

methods are often used. Since the original proposal (LB) by Le Roy and Bernstein [25], this general approach has been used in numerous contexts, including a determination of the asymptotic limit of the $B^1\Sigma_u^+$ state of H_2 [36], recent fits to data on the Rb_2 $0_u^+(5\,^2P_{1/2})$ [37], and $0_g^-(5\,^2P_{1/2})$ [38] states, as well as an analysis of the pure long range Cs_2 $0_g^-(6\,^2P_{3/2})$ state [26]. It appears logical to consider such approaches here. However, the results are not completely satisfactory when compared to the eigenvalue calculation discussed below.

A reduction of the NDE problem to one channel in a low-order approximation makes use of an analytic expansion of the potential $V(R)$. Low-order expansions for various electronic states below a $^2S + {}^2P$ limit are given analytically in Table V of Ref. [26]. The first such term in R^{-3} for the $Rb_2\,{}^3\Sigma_{1g}(2P_{1/2})/(1)1_g$ state is

$$V(1)[1_g] = D_L - 2\frac{C_3}{R^3} + \cdots, \quad C_3 = \langle 5s|r|5p\rangle(1+\epsilon), \quad (8)$$

where D_L is the dissociation limit, and ϵ is a relativistic correction in the order of 3×10^{-4} [39] that will generally be ignored here. In the following, the terms following $-2C_3/R^3$ also will be small enough to be ignored.

The original LB model [25] for a potential of the form $V(R) = D - C_{3,\mathrm{eff}}/R^3$, yields the following expression for vibronic energies $E(v)$:

$$v_D - v = \frac{4a_3}{h}\sqrt{2\mu}C_{3,\mathrm{eff}}^{1/3}[D - E(v)]^{1/6} = K[D - E(v)]^{1/6};$$
$$a_3 = \frac{\sqrt{\pi}\,\Gamma(5/6)}{2\Gamma(4/3)} = 1.1202513, \quad (9)$$

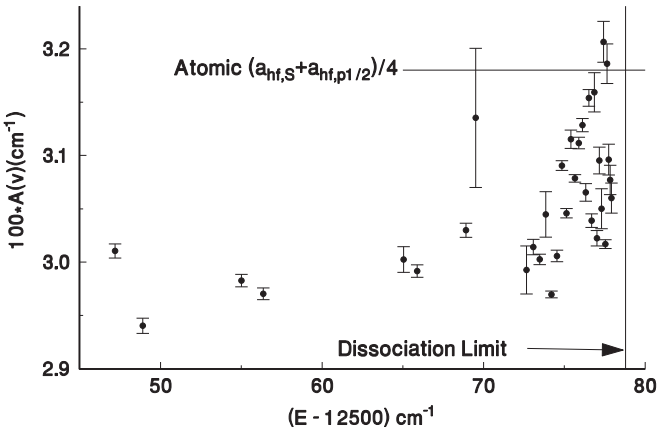

FIG. 3. A plot of the fitted molecular hyperfine parameters $A(v)$ (times 100, in cm^{-1}), vs. vibrational energy. The error bars denote three standard deviations of the fitted parameters.

where μ is the molecular reduced mass, the Γ's are Gamma functions, and v_D is the asymptotic vibrational quantum number. If D and $E(v)$ are in cm^{-1} and $C_{3,\mathrm{eff}}$ is in atomic units, then for $^{87}Rb_2$, K (in $[\mathrm{cm}^{-1}]^{-1/6} = 35.7093\, C_3^{1/3}$), where C_3 is in atomic units. For C_n, the atomic unit is $E_H a_0^n$, where $E_H = 4.3597442 \times 10^{-18}$ J, and $a_0 = 5.29177211 \times 10^{-11}$m.

When the 25 highest $G(v)$ values in Table I were used in a fit to the above expression to obtain values for the parameters v_D, D_L, and K, the resulting value for C_3 was 12.1% less than the accurate value obtained from lifetime measurements, as given in Ref. [39]. In view of this discrepancy, we then considered the improved Le Roy-Bernstein models of Comparat [26]. The first such improvement involved simply adding a term $\gamma(E(v) - D_L)$ to the above expression for $v_D - v$, where γ is a small parameter to be fitted from the data. With this model, a fit to the top 25 $G(v)$ values, using the C_3 value from Ref. [39], was much improved over the results cited previously. The residuals from this fit are shown in Table I, column δ_a. Large deviations for levels below $v' = 26$ indicate that higher-order dispersion terms might be useful. We also note that the fitted value for v_D, the effective vibrational quantum number at the asymptotic limit, was unreasonably large ($v' = 114.5$) as is said to be typical of NDE approaches [26].

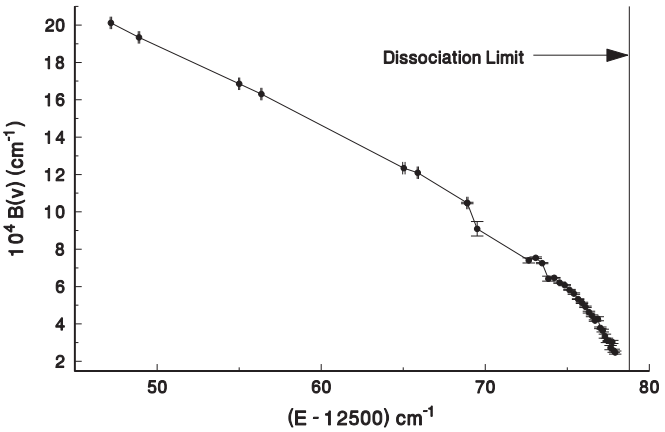

FIG. 4. A plot of the fitted molecular rotational parameters $B(v)$ times 10^4, in cm^{-1}, vs. vibrational energy. Error bars denote 3σ uncertainties.

Th extension of the LB model to include the C_6 as well as C_3 coefficient was considered by Le Roy [40]. However, the required integrals for the case of $n,m = 3,6$ diverged. More recently, Comparat [26] has presented another approach to this problem. His expression can be written

$$v_D - v = W = K[D - E(v)]^{1/6} + \gamma[D - E(v)] + \frac{5K}{42}\frac{C_6}{C_3}[D - E(v)]^{7/6}, \tag{10}$$

where as given above, K includes a factor $C_{3,\mathrm{eff}}^{1/3}$. One problem with this formulation is that it is difficult to invert Eq. (10) to obtain values for $E(v)$ for direct comparison with observations. To make such comparisons, we have calculated $dE(v)/dv$ for each observed level (using the numerical potential fit), and then multiplied this quantity by $v_D - v - W$ to obtain values for the effective residual δ_b as given in Table I. In this case, all observed levels were included in the fit. The results are useful, but, again, not on a par with the numerical eigenvalue results discussed below. It may be that the semiclassical approximation itself, which is necessarily employed in NDE methods, limits the accuracy.

For a numerical approach employing a fitted potential, we consider that the $1_g(P_{1/2})$ state is coupled by spin-orbit interactions to the $^1\Pi_g(P_{3/2})$ and $^3\Pi_g(P_{3/2})$ states, both of which evolve to 1_g states in the large R limit, as shown in Fig. 1. The Hamiltonian matrix for the long range potential functions for these three $\Omega = 1_g$ states, relative to the center of gravity of the $5\,^2S + 5\,^2P$ manifold, is

$$\begin{array}{c} {}^3\Sigma_{1g} \\ {}^1\Pi_{1g} \\ {}^3\Pi_{1g} \end{array} \begin{pmatrix} V(^3\Sigma_{1g}) & \Delta & \Delta \\ \Delta & V(^1\Pi_{1g}) & -\Delta \\ \Delta & -\Delta & V(^3\Pi_{1g}) \end{pmatrix}, \tag{11}$$

where $\Delta = 79.200\ \mathrm{cm}^{-1}$ [30] is the spin-orbit parameter (one-third the $5\,^2P$ atomic fine structure splitting). The potentials in Eq. (11) are [41,42]

$$V(^3\Sigma_{1g}) = -f^{\Sigma}\frac{2C_3}{R^3} - \frac{C_6^{\Sigma}}{R^6} - \frac{C_8(^3\Sigma_g^+)}{R^8}, \tag{12}$$

$$V(^1\Pi_{1g}) = -f^{\Pi}\frac{C_3}{R^3} - \frac{C_6^{\Pi}}{R^6} - \frac{C_8(^1\Pi_g)}{R^8}, \tag{13}$$

$$V(^3\Pi_{1g}) = f^{\Pi}\frac{C_3}{R^3} - \frac{C_6^{\Pi}}{R^6} - \frac{C_8(^3\Pi_g)}{R^8}. \tag{14}$$

In the above, the small retardation corrections [43] are [$\lambda\!\!\!^{-} = (1/2\pi)$ times the $5\,^2S \to 5\,^2P_{1/2}$ excitation wavelength]

$$f^{\Sigma} = \cos\left(\frac{R}{\lambda\!\!\!^{-}}\right) + \left(\frac{R}{\lambda\!\!\!^{-}}\right)\sin\left(\frac{R}{\lambda\!\!\!^{-}}\right); \quad \lambda\!\!\!^{-} = \frac{\lambda_{\mathrm{res}}}{2\pi}; \tag{15}$$

$$f^{\Pi} = \cos\left(\frac{R}{\lambda\!\!\!^{-}}\right) + \left(\frac{R}{\lambda\!\!\!^{-}}\right)\sin\left(\frac{R}{\lambda\!\!\!^{-}}\right) - \left(\frac{R}{\lambda\!\!\!^{-}}\right)^2\cos\left(\frac{R}{\lambda\!\!\!^{-}}\right), \tag{16}$$

where λ_{res} is the wavelength on resonance for the $^2 5S \to 5\,^2P$ transition, averaged over the fine structure components.

Our numerical potential model employs the *ab initio* potential from [16], (two) harmonic correction terms for $R < R_e$ and $R \sim R_e$, where R_e is the internuclear distance

TABLE II. Parameters from fits to the experimental data, and from previous work. R_x and V_x refer to the transition point between the adjusted *ab initio* potential and the long-range potential, in the potential fit. The C_n coefficients are all in atomic units. Pot. fit = potential fit in this work. W.M. = weighted mean of four atomic hfs limits, as discussed in the text.

Parameter	Value	Source
R_x	16.0 Å	Pot. Fit
V_x	12501.0 cm^{-1}	Pot. Fit
V_{dis}	12578.782 cm^{-1}	Pot. Fit
V_{dis}	12578.790 cm^{-1}	W.M. [30]
C_3	9.202	Th. [41]
C_3	8.784(6)	Exp. [23]
C_3	8.905(26)	Exp. [39]
C_3	8.903	Exp. [24]
C_6^{Σ}	1.205×10^4	Th. [41]

at the potential minimum, and a long-range part, for $R > R_x$. The long-range part employed the lowest eigenvalue, $E_1(R)$, from the above matrix, Eq. (11). R_x was eventually chosen to be 16 Å to optimize the fit to all the $G(v)$ data, after numerous trials. Because the *ab initio* potential varied with R nearly as $E_1(R)$, it was sufficient to shift the *ab initio* potential for all $R \leqslant R_x$ by a constant ΔV. The C_3 and C_6 parameters were taken at their accepted values from Refs. [39,41], as given in Table II. This potential was optimized to reproduce the $G(v')$ data of Table I and to the extent possible, the data of Ref. [12] for 1_g levels for $v = 0 \leqslant 16$. Data exist also for some intermediate levels shown in Refs. [13,44]. However, the gap of 1500 cm^{-1} between the data of [12,13,44], and the absence of $B(v)$ information from these data sets made it problematic to obtain an overall 1_g potential that could simulate all the available data. Nonetheless, $G(v)$ values for the 33 levels listed in Table I could be reproduced to better accuracy than obtained with the NDE expansions. The residuals obtained in such a fit are given in Table I in the column labeled "δ_{pf}." With one exception, they are less than 0.012 cm^{-1}. We have not been able to identify the reason for this one exception, although one expects perturbations from states of other symmetry (0_g^-,0_u^+, etc.).

The dissociation limit was a fitted parameter here. The result, given in Table IV B, 12578.782 cm^{-1}, may be compared to the difference between ^{87}Rb $5\,^2P_{1/2}(F = 1)$ and ^{87}Rb $5\,^2S_{1/2}(F = 2)$, namely 12578.8485 cm^{-1}, from Ref. [30]. However, as the molecule approaches the dissociation limit, the representation in terms of a Hund's case (c) molecular potential must be transformed to the various possible combinations of free atom hyperfine states for $^2S + {}^2P_{1/2}$ ^{87}Rb atoms. Since $J = 1/2$ and $I = 3/2$ in each case, one has $F = 1$ and 2 states for both ^2S and $^2P_{1/2}$ atoms, and thus four possibilities. Figure 5 displays the highest observed $G(v)$ values and the fit results up to the dissociation limit together with horizontal lines that denote the four possible free atom states, relative to the initial $^2S_{1/2}(F = 2) + {}^2S_{1/2}(F = 2)$ atomic energy. The fitted effective dissociation limit lies in between the four possible free atom limits. An average of these four limits, each weighted by $(2F'' + 1)(2F' + 1)$, is found to be 12578.7900 cm^{-1},

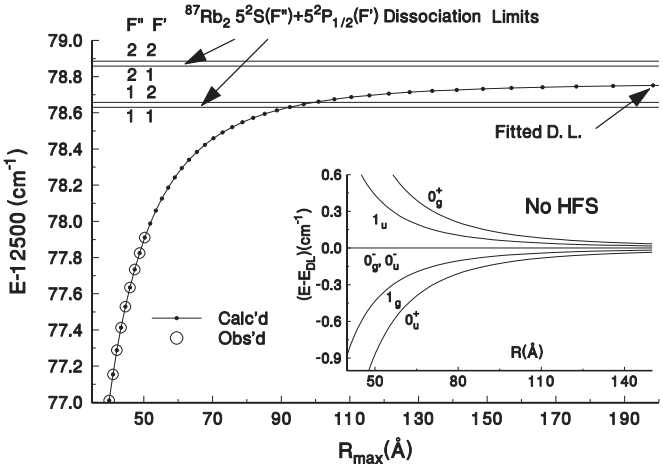

FIG. 5. This plot shows the highest observed $G(v)$ values (circles) together with the fitted energies (solid dots, thicker solid line), together with the calculated F'', F' energies or dissociation limits relative to the $5\,^2S_{1/2}(F'' = 2) + 5\,^2S_{1/2}(F'' = 2)$ initial state. The inset shows the molecular potentials converging also to the $5\,^2S_{1/2} + 5\,^2P_{1/2}$ limit, in accord with the Movre-Pichler [27] model.

which differs by only 0.008 cm^{-1} from the fitted dissociation limit parameter.

Also shown in an inset in this figure are all the Hund's case (c) molecular states that dissociate to this limit according to the classic Movre-Pichler (MP) model [27]. One can calculate a transformation between the atomic limit with hyperfine structure and the molecular MP potentials, and it appears that the 1_g molecular state would be distributed over all four atomic hyperfine states. Since g/u parity does not apply in the atomic limit, this transformation effectively couples g and u states, and singlet and triplet states, as in the case of the $X\,^1\Sigma_g^+$ and $a\,^3\Sigma_u^+$ states of Cs_2 in Ref. [45]. A discussion of the details is beyond the scope of this work since the analysis of the experimental data could not be extended into the highly congested spectral region near the dissociation limit. The fitted potential is given numerically in the supplementary data file [35]. The $T(0)$ value is within 1 cm^{-1} of the observed $G(0)$ value from Ref. [12].

In conclusion, we state again that a judicious selection of laser polarizations applied to cold atoms in a FORT has been used to simplify molecular hyperfine structure. Together with high resolution data collection, this has facilitated analysis of rotational, vibrational, and hyperfine structure in levels of the Rb_2 $1_g(P_{1/2})$ near the dissociation limit. Transitions are observed for only one value of the total nuclear spin I, and also only one value of the rotational angular momentum ℓ. The vibrational energies, applied to a numerical eigenvalue calculation for a potential based on a shifted *ab initio* potential [16] spliced on to the long-range part, in turn confirm previous determinations of the C_3 and C_6 dispersion coefficients as they apply to this particular state. To obtain this agreement, it was essential to consider couplings at large internuclear distance between the three 1_g states dissociating to Rb5 $^2S + $ Rb5 ^2P. Application of NDE expansion methods yields useful results, but not of the quality of the numerical eigenvalue calculation. It remains to better bridge the gap between the data presented here and the published data on low-lying levels of this state [12].

The emphasis in this study has been on the hyperfine and vibrational structure of the $Rb_2 1_g(5P_{1/2})$ levels near the dissociation limit because the experimental approach provided such clearly resolved data. We have made only an approximate fit to data on lower levels of the 1_g state. In the future, we hope to carefully compile all available data on the $Rb_2\,^3\Sigma_g^+(5P_{1/2})$ state and produce an empirical potential that better reproduces the available data from more deeply bound states. Perhaps it would be possible also to identify the perturbing states that displace the $A(v)$ values shown in Fig. 3, and then model the perturbation effects quantitatively.

ACKNOWLEDGMENTS

The work at the University of Texas was supported by NSF and by the R. A. Welch Foundation. The work at Stony Brook was supported by NSF Grant No. PHY-0968905. We gratefully acknowledge comments by O. Dulieu, LAC, Orsay, who emphasized the accuracy of the C_3 value from Ref. [39], and inspired a more thorough approach to the eigenvalue calculation. T. Takekoshi and J. Hecker Denschlag provided useful, more detailed information on the data in Ref. [12]

[1] K. M. Jones, E. Tiesinga, P. D. Lett, and P. S. Julienne, Rev. Mod. Phys. **78**, 1041 (2006).
[2] O. Dulieu and C. Gabbanini, Rep. Prog. Phys. **72**, 086401 (2009).
[3] J. Ulmanis, J. Deiglmayr, M. Repp, R. Wester, and M. Weidemüller, Chem. Rev. **112**, 4890 (2012).
[4] G. Quémémener and P. S. Julienne, Chem. Rev. **112**, 4949 (2012).
[5] C. J. Williams and P. S. Julienne, J. Chem. Phys. **101**, 2634 (1994).
[6] X. Wang, H. Wang, P. L. Gould, W. C. Stwalley, E. Tiesinga, and P. S. Julienne, Phys. Rev. A **57**, 4600 (1998).
[7] M. Kemmann, I. Mistrik, S. Nussmann, H. Helm, C. J. Williams, and P. S. Julienne, Phys. Rev. A **69**, 022715 (2004).
[8] C. D. Hamley, E. M. Bookjans, G. Behin-Aein, P. Ahmadi, and M. S. Chapman, Phys. Rev. A **79**, 023401 (2009).
[9] D. Comparat, C. Drag, B. Laburthe Tolra, A. Fioretti, P. Pillet, A. Cruvellier, O. Dulieu, and F. Masnou-Seeuws, Eur. Phys. J. D **11**, 59 (2000).
[10] D. Wang, J. Qi, M. F. Stone, O. Nikolayeva, B. Hattaway, S. Gensemer, H. Wang, W. T. Zemke, P. L. Gould, E. E. Eyler, and W. C. Stwalley, Eur. Phys. J. D **31**, 165 (2004).
[11] A. J. Kerman, J. M. Sage, S. Sainis, T. Bergeman, and D. DeMille, Phys. Rev. Lett. **92**, 033004 (2004).
[12] T. Takekoshi, C. Strauss, F. Lang, J. H. Denschlag, M. Lysebo, and L. Veseth, Phys. Rev. A **83**, 062504 (2011).
[13] J. D. Miller, R. A. Cline, and D. J. Heinzen, Phys. Rev. Lett. **71**, 2204 (1993).
[14] J. R. Gardner, R. A. Cline, J. D. Miller, D. J. Heinzen, H. M. J. M. Boesten, and B. J. Verhaar, Phys. Rev. Lett. **74**, 3764 (1995).
[15] S. J. Park, S. W. Suh, Y. S. Lee, and G.-H. Jeung, J. Mol. Spectrosc. **207**, 129 (2001).
[16] M. Aubert-Frécon (private communication) (2007).
[17] C. Gabbanini, A. Fioretti, A. Lucchesini, S. Gozzini, and M. Mazzoni, Phys. Rev. Lett. **84**, 2814 (2000).
[18] A. Fioretti, C. Amiot, C. M. Dion, O. Dulieu, M. Mazzoni, G. Smirne, and C. Gabbanini, Eur. Phys. J. D **15**, 189 (2001).
[19] J. Lozeille, A. Fioretti, C. Gabbanini, Y. Huang, H. K. Pechkis, D. Wang, P. L. Gould, E. E. Eyler, W. C. Stwalley, M. Aymar, and O. Dulieu, Eur. Phys. J. D **39**, 261 (2006).
[20] Y. Huang, J. Qi, H. K. Pechkis, D. Wang, E. E. Eyler, P. L. Gould, and W. C. Stwalley, J. Phys. B **39**, S857 (2006).
[21] F. Lang, K. Winkler, C. Strauss, R. Grimm, and J. Hecker Denschlag, Phys. Rev. Lett. **101**, 133005 (2008).
[22] A. N. Drozdova, A. V. Stolyarov, M. Tamanis, R. Ferber, P. Crozet, and A. J. Ross, Phys. Rev. A **88**, 022504 (2013).
[23] R. A. Cline, J. D. Miller, and D. J. Heinzen, Phys. Rev. Lett. **73**, 632 (1994).
[24] T. Bergeman, J. Qi, D. Wang, Y. Huang, H. Pechkis, E. E. Eyler, P. L. Gould, W. C. Stwalley, R. A. Cline, J. D. Miller, and D. J. Heinzen, J. Phys. B **39**, S813 (2006).
[25] R. J. Le Roy and R. B. Bernstein, J. Chem. Phys. **52**, 3869 (1970).
[26] D. Comparat, J. Chem. Phys. **120**, 1318 (2004).
[27] M. Movre and G. Pichler, J. Phys. B **10**, 2631 (1977).
[28] J. Brown and A. Carrington, *Rotational Spectroscopy of Diatomic Molecules* (Cambridge University Press, Cambridge, England, 2003).
[29] H. Salami, T. Bergeman, B. Beser, J. Bai, E. H. Ahmed, S. Kotochigova, A. M. Lyyra, J. Huennekens, C. Lisdat, A. V. Stolyarov, O. Dulieu, P. Crozet, and A. J. Ross, Phys. Rev. A **80**, 022515 (2009).
[30] D. A. Steck, "Rubidium 87 D Line Data," available online at http://steck.us/alkalidata (revision 2.1.4, 23 December 2010).
[31] E. Arimondo, M. Inguscio, and P. Violino, Rev. Mod. Phys. **49**, 31 (1977).
[32] R. W. Heather and P. S. Julienne, Phys. Rev. A **47**, 1887 (1993).
[33] S. J. Singer, K. F. Freed, and Y. B. Band, J. Chem. Phys. **79**, 6060 (1983).
[34] R. N. Zare, *Angular Momentum* (John Wiley & Sons, New York, 1988).
[35] See Supplemental Material at http://link.aps.org/supplemental/10.1103/PhysRevA.88.052509 for more information on the fitted potential.
[36] W. C. Stwalley, Chem. Phys. Lett. **6**, 241 (1970).
[37] H. Jelassi, B. Viaris de Lesegno, and L. Pruvost, Phys. Rev. A **73**, 032501 (2006).
[38] H. Jelassi, B. V. de Lesegno, and L. Pruvost, Phys. Rev. A **74**, 012510 (2006).
[39] R. F. Gutterres, C. Amiot, A. Fioretti, C. Gabbanini, M. Mazzoni, and O. Dulieu, Phys. Rev. A **66**, 024502 (2002).
[40] R. J. Le Roy, J. Chem. Phys. **73**, 6003 (1980).
[41] M. Marinescu and A. Dalgarno, Phys. Rev. A **52**, 311 (1995).
[42] T. Bergeman, P. S. Julienne, C. J. Williams, E. Tiesinga, M. R. Manaa, H. Wang, P. L. Gould, and W. C. Stwalley, J. Chem. Phys. **117**, 7491 (2002).
[43] W. J. Meath, J. Chem. Phys. **48**, 227 (1968).
[44] J. Miller, Ph.D. Thesis, University of Texas at Austin, 1994.
[45] S. Sainis, J. Sage, E. Tiesinga, S. Kotochigova, T. Bergeman, and D. DeMille, Phys. Rev. A **86**, 022513 (2012).